

q-scatter: Numerical Framework for Fast Prediction of Particle Distributions in Electron-Laser Scattering

Óscar Amaro , Marija Vranic 

GoLP/Instituto de Plasmas e Fusão Nuclear, Instituto Superior Técnico, Universidade de Lisboa, 1049-001 Lisbon, Portugal

E-mail: oscar.amaro@tecnico.ulisboa.pt , marija.vranic@tecnico.ulisboa.pt

Abstract.

The new generation of multi-PetaWatt laser facilities will allow tests of Strong Field QED, as well as provide an opportunity for novel photon and lepton sources. The first experiments are planned to study the (nearly) head-on scattering of intense, focused laser pulses with either relativistic electron beams or high-energy photon sources. In this work, we present a numerical framework that can provide fast predictions of the asymptotic particle and photon distributions after the scattering. The works presented in this manuscript includes multiple features such as spatial and temporal misalignment between the laser and the scattering beam, broadband electron beams, and beam divergence. The expected mean energy, energy spread, divergence or other observables are calculated by combining an analytical description and numerical integration. This method can provide results within minutes on a personal computer, which would otherwise require full-scale 3D QED-PIC simulations using thousands of cores. The model, which has been compiled into an open-source code **q-scatter**, may be used to support the analysis of large-size data sets from high-repetition rate experiments, leveraging its speed for optimization or reconstruction of experimental parameters.

1. Introduction

Strong-field quantum electrodynamics (SFQED) is a rapidly developing research field that studies the interaction between matter and intense electromagnetic fields. In recent years, there has been a growing interest in this area due to the availability of high-intensity laser sources, which enable the exploration of novel physical phenomena, with experiments being planned for the near future: ELI [1], Apollon [2], CoReLS [3], FACET-II [4, 5], LUXE [6, 7], EXCELS [8], ZEUS [9], Omega Laser Facility [10], HIBEF [11], among others. The proposed experimental setups consist of scattering of intense, focused laser pulses with either relativistic electron beams or high-energy photons, allowing for precision studies of radiation reaction (the recoil on the charged particles that emit high-energy photons) and electron-positron production in the lab.

In these studies, different regimes of radiation reaction can be identified based on the energies of the probe particles and the strength of the electromagnetic fields involved.

Recent experiments have demonstrated electron energy loss that can be attributed to radiation reaction [12, 13]. For low enough electron energies and laser intensities, the effect of radiation on the radiation emitting electrons can be described through a continuous correction to the equation of motion, e.g. the Landau-Lifshitz equation [14]. For intermediate values of energies and intensities, the evolution of the particle distribution can be modeled by a Fokker-Planck equation, where the energy of each emitted photon is assumed to be much smaller than the emitting lepton [15, 16]. In this case, the particle can still lose a significant fraction of its energy through multiple emissions of low-energy photons. For higher energies and intensities, a single photon emission can lead to almost complete energy depletion of the parent lepton, and thus a Boltzmann/transport equation becomes a better description. A comparison between the different models of radiation reaction and their range of validity can be found in the recent literature [17–19].

Besides radiation reaction, a phenomena likely to occur in electron-laser collisions is Breit-Wheeler [20] electron-positron pair production. The pair production rates for this process are known for particles in a constant intense background field, and can be mapped onto a plane wave scenario. There are also extended models that take into account the fact that the laser is a wavepacket with a temporal envelope. For example, the authors in Ref. [21] derive approximate scaling laws for the expected positron yield for both photon-laser and electron-laser collisions. Further theoretical work was pursued by [22], where the authors investigated photon-laser scattering for different Laguerre-Gauss modes of the laser, and in [23] where optimal focusing conditions were found for maximizing the number of pairs from the scattering between Gaussian laser pulses and different electron beam profiles.

Since the strong-field regime of QED is characterized by the breakdown of perturbative approaches, it requires the development of new theoretical and computational tools. Numerical modeling of experiments with enough spatiotemporal resolution and accounting for all relevant scattering parameters becomes too computationally expensive if relying on full-scale 3D PIC and Monte Carlo simulations, especially if the analysis requires multiple parameter studies. New methods are currently being evaluated for accelerating the evaluation of QED rates (e.g. Machine-Learning based [24], and Chebyshev polynomial fits [25]).

In this paper, we describe the development of a reduced semi-analytical model for the final energy and angular distribution of particles in electron-laser scattering (see figure 1). This approach simplifies the calculation for various beam geometries, focusing and collision synchronization. The results can be obtained within minutes on a personal computer. We perform benchmarks with the fully-relativistic particle-in-cell code OSIRIS [26], and demonstrate that with this model quantitative predictions can be obtained without the need for the full-scale simulations. This can be particularly useful for real-time parameter scans during the course of an experiment.

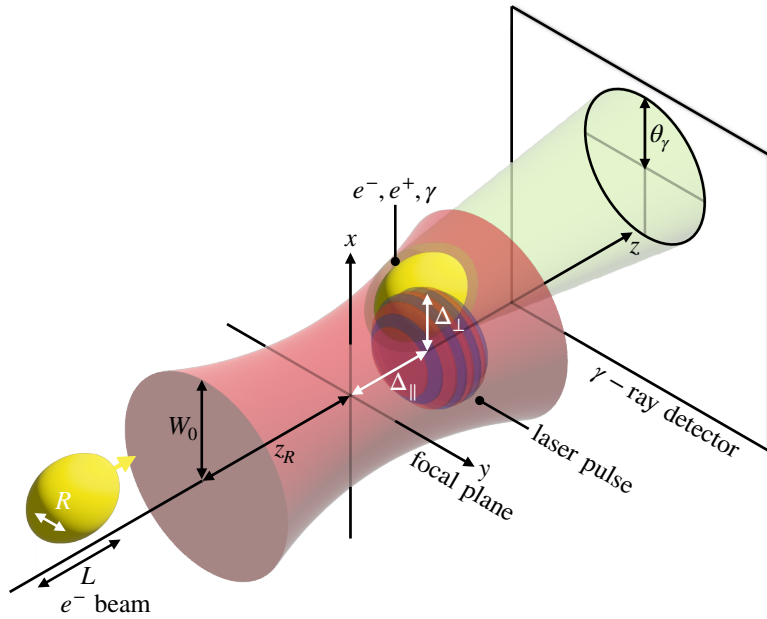


Figure 1: Scattering of a relativistic electron beam (yellow) and a counter-propagating laser pulse (red and blue). Electron-positron pairs and high energy photons can be produced in the interaction, and their number, spectra and divergence will depend on the precise geometry of the collision.

This manuscript is structured as follows. In section 2, we discuss the mapping between plane wave (PW) models and more realistic “3D” scattering setups. In section 3, we use this approach to derive the final spectra of photons and electrons after scattering with a finite, focused laser pulse. In section 4, we apply an approximate semi-classical numerical model for the photon energy distribution. In section 5, we investigate the electron and photon angular distribution as well as positron yield. Finally, the conclusions are presented in section 6.

2. Effective intensity in focused laser scattering

This section introduces the theoretical framework for describing the distribution of particles in the maximum effective intensity of the laser they interact with along their ballistic trajectories. This approach aims at simplifying the mapping between 1D plane wave models to more realistic 3D-focused-laser environments.

To better understand the derivation of the effective intensity distribution, it is useful to first recall the case of a plane wave pulse. When a beam of particles collides with this laser pulse (there is no focusing, the wavepacket has a temporal envelope and no transverse structure), all particles get to interact with the maximum intensity. For this case, the distribution of particles dN_b according to the peak laser vector potential they interact with $a_{0,\text{eff}}$ is of the form $dN_b/da_{0,\text{eff}} \sim \delta(a_{0,\text{eff}} - a_0)$, as all particles experience the maximum vector potential a_0 .

However, in the case of a diffraction-limited focused laser, not all beam particles (which can be either ultra-relativistic electrons or photons) interact with the peak laser intensity, but rather with a maximum $a_{0,\text{eff}}$ that depends on the longitudinal and transverse offsets from the focus at the collision time. If one considers a cylindrical coordinate system $\vec{r} = (\rho, \phi, z)$, each beam particle is assigned an effective vector potential $a_{0,\text{eff}}(\rho, \phi, z)$ according to the distribution function

$$\frac{dN_b}{da_{0,\text{eff}}} (a_{0,\text{eff}}) = \int_V 2 \delta(a(\vec{r}) - a_{0,\text{eff}}) n_b(\vec{r}) dV = \int_S \frac{2 n_b dS}{||\nabla a||}. \quad (1)$$

where $a_{0,\text{eff}}$ is the argument of the distribution function, $a(\vec{r})$ is the effective vector potential as a function of the coordinates (to be specified later), n_b is the particle number density in the lab frame, the factor 2 accounts for crossing time (at twice the speed of light for ultrarelativistic particles), and the surface integral (right-hand side) is evaluated at $a = a_{0,\text{eff}}$. The functional expression above assigns each macro-particle (which is equivalent to a volume element in the electron distribution) a spatial coordinate corresponding to the position along its trajectory where it interacts with the maximum laser field. The volumetric integral then assigns the volume element to the correct bin in the $a_{0,\text{eff}}$ distribution. As a Gaussian focusing geometry is cylindrically symmetric around the laser propagation axis, we can convert equation (1) to a surface integral, where $dS = \rho \sqrt{d\rho^2 + dz^2} d\varphi = \rho \sqrt{1 + (\partial\rho/\partial z)^2} dz d\varphi$ is calculated at the isosurface that is by definition perpendicular to the gradient of the vector potential given by $||\nabla a|| = \sqrt{(\partial a/\partial \rho)^2 + (\partial a/\partial z)^2}$.

The distribution becomes a function of both the beam density profile and the laser's spatial structure (neglecting the wave's phase, and in particular its wavefront curvature). For example, the ideal Gaussian laser has a spatial dependence

$$a(\rho, \phi, z) = \frac{a_0}{\sqrt{1 + (z/z_R)^2}} \exp\left(-\frac{\rho^2/W_0^2}{1 + (z/z_R)^2}\right) \quad (2)$$

where W_0 is the spotsize, $z_R \equiv \pi W_0^2/\lambda$ the Rayleigh length, and λ is the laser central wavelength.

For an arbitrary beam density profile $n_b(\vec{r})$ with length L and radius R , it can be challenging to analytically compute the particle distribution in $a_{0,\text{eff}}$. However, in the limiting cases of a Short beam ($L \ll z_R$, transverse Gaussian density), Wide beam ($R \gg W_0$, longitudinal and transverse flat-top density) and Thin beam ($R \ll W_0$, longitudinal flat-top density) these distributions can be calculated. In figure 2, we present several instances of these geometries and their respective distributions. In table 1, we collect the distributions for the three above-mentioned geometries, generalized to the case of non-synchronized scattering, i.e., when the particle beam and laser collide outside of the focus.

Setup Particle distribution for temporally unsynchronized beams

Wide beam
$$\frac{dN_b}{da} = \frac{2\pi n_b W_0^2 z_R}{a} \left(\frac{z_+}{z_R} \left(1 + \frac{1}{3} \left(\frac{z_+}{z_R} \right)^2 \right) \theta(a_{z_+} - a) - \frac{z_-}{z_R} \left(1 + \frac{1}{3} \left(\frac{z_-}{z_R} \right)^2 \right) \theta(a_{z_-} - a) \right. \\ \left. + \frac{\sqrt{a_0^2 - a^2}}{3 a} \left(2 + \frac{a_0^2}{a^2} \right) (\theta(a - a_{z_+}) \pm \theta(a - a_{z_-})) \right)$$

Thin beam
$$\frac{dN_b}{da} = \frac{2N_b z_R}{L} \frac{a_0^2}{a^2} \frac{1}{\sqrt{a_0^2 - a^2}} (\theta(a - a_{z_+}) \pm \theta(a - a_{z_-}))$$

Short beam
$$\frac{dN_b}{da} = N_b \frac{W^2}{R^2} \frac{1}{a} \left(\frac{a}{a_0} \frac{W}{W_0} \right)^{W^2/R^2} I_0 \left(2 \frac{\Delta_\perp}{R} \frac{W}{R} \log^{1/2} \left(\frac{a_0}{a} \frac{W_0}{W} \right) \right) \exp \left(-\frac{\Delta_\perp^2}{R^2} \right) \theta(a - a_{\parallel})$$

Table 1: Particle distributions for arbitrary temporal synchronization. A shorter notation is used $a \equiv a_{0,\text{eff}} < a_0$. Here, $a_z \equiv a_0 / \sqrt{1 + (L/4z_R)^2}$ is the $a_{0,\text{eff}}$ associated with the integration limits imposed by the longitudinal size of the electron beam, N_b represents the total number of particles in the beam, n_b is the beam density, R and L are the beam radius and length respectively. The laser spot size is W_0 in the focal plane and $W = W_0 \sqrt{1 + \Delta_\parallel^2/z_R^2}$ outside, $z_R \equiv \pi W_0^2 / \lambda$ is the Rayleigh length, and Δ_\parallel , Δ_\perp are the displacements of the collision center from the laser propagation axis and focal plane, respectively. The \pm sign corresponds to situations where $\Delta_\parallel < L/4$ or $\Delta_\parallel > L/4$ respectively, $\theta(x)$ is the Heaviside Theta function, $z_\pm = \Delta_\parallel \pm L/4$, $a_{z_\pm} = a_0 / \sqrt{1 + (z_\pm/z_R)^2}$ and $a_{\parallel} = a_0 / \sqrt{1 + (\Delta_\parallel/z_R)^2}$.

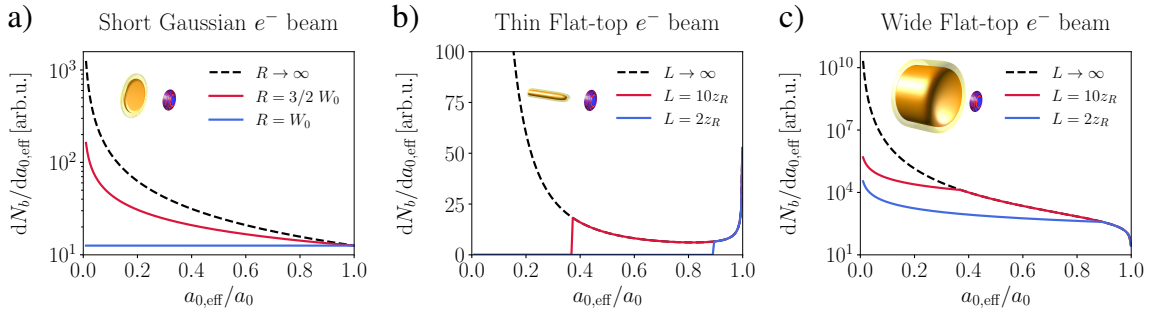


Figure 2: Particle distributions for different geometries, where $\lambda = 1 \mu\text{m}$ and $W_0 = 2 \mu\text{m}$. The dashed line corresponds to the limit of either infinite beam radius (Short beam) or infinite length (Thin and Wide beams).

We first introduced the concept of the $dN_b/da_{0,\text{eff}}$ distribution in our previous work [23], where we applied it to the optimization of the number of pairs produced in electron-laser scattering. We accomplished that by generalizing the scaling law previously derived for positron production in a plane wave [21]. This approach is cost-effective and amenable to analytical calculations pairing with PW models for other observables. In the next section, we apply our method to estimate the final electron energy spectrum in a focused laser scattering.

3. Electron and photon spectra

In this section, we apply the effective interaction intensity distributions to derive the asymptotic energy distributions of the electrons after the scattering. Simulation parameters for the given examples can be found in appendix 7.

3.1. Classical Radiation Reaction

If the scattering between the laser and the electron beam is in the classical regime of interaction, one can assign a deterministic trajectory to an electron within the beam. If there is considerable radiation emission (e.g. a few percent of the electron energy is radiated) during the interaction, then we can describe the motion through the Landau-Lifshitz equation, which has an exact solution in a plane wave [27]. This solution calculates the full space-time trajectory of the particle as it interacts with the laser field (in configuration and momentum space). For the case of a pulse with a temporal envelope, this solution can be condensed into a scaling law for the final energy of the electron [28]

$$\gamma_f = \frac{\gamma_0}{1 + c_{RR} \frac{\gamma_0}{\omega_0^2} a_0^2}, \quad c_{RR} \equiv (1 - \cos \theta)^2 \frac{\eta e^2 \omega_0^2}{3 m c^3} \tau_0. \quad (3)$$

Here, γ_0 is the initial electron energy, τ_0 is the laser pulse duration, ω_0 the fundamental laser frequency, c_{RR} is a numerical factor quantifying radiation reaction that depends on the laser shape and scattering angle, η is a numerical factor associated with the temporal shape of the laser pulse, θ is the interaction angle between the laser wavefront and the colliding electron, e is the elementary electric charge, m the electron mass, and c is the speed of light in vacuum.

Equation (3) shows a 1-to-1 relation between the final energy and the a_0 of the plane wave (fixing all other parameters), which means it is possible to directly calculate the final energy for each particle, provided we know the maximum laser intensity and γ_0 . Combining the effective intensity distributions from table 1 and the equation (3), we obtain the full energy distribution function after the interaction

$$\frac{dN_b}{d\gamma_f}(\gamma_f) = \frac{dN_b}{da_{0,\text{eff}}} \left(\frac{d\gamma_f}{da_{0,\text{eff}}} \right)^{-1} \quad (4)$$

where the second part is the inverse of the derivative of equation 3 with $a_0 = a_{0,\text{eff}}$. In figure 3, we compare the distributions obtained from the analytical expression (4) against PIC simulations. Here, electrons radiate energy following the Landau-Lifschitz classical radiation reaction model, while the quantum radiation reaction/QED module was turned off in the simulation parameters to demonstrate the applicability of the model. For the different geometries and aspect ratios R/W_0 , we find good agreement between the predicted distributions and simulation results. It is worth noting that the cut-offs in the spectra (specially for the Short and Thin beams) is a feature of deterministic radiation reaction; however, this will be smoothed out if the initial electron beam has large enough energy spread or a stochastic quantum radiation reaction model is used.

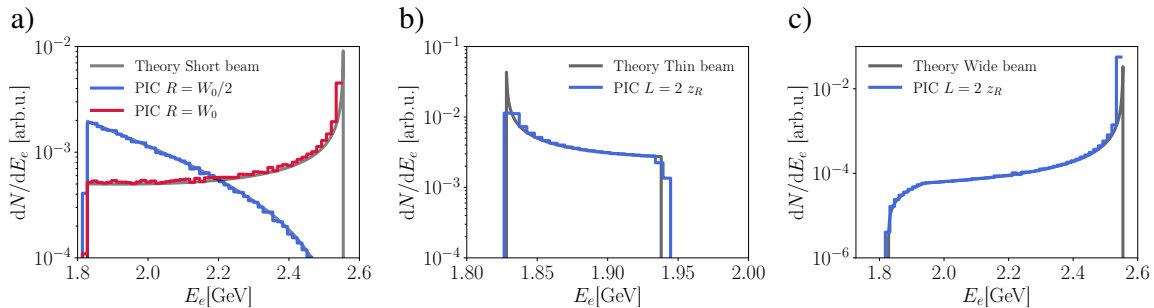


Figure 3: Final electron energy distributions for Short, Thin and Wide beam geometries after classical radiation reaction. Parameters: $\gamma_0 = 5000$, $a_0 = 12$, $\lambda = 0.8 \mu\text{m}$, $\tau_0 = 50 \omega_0^{-1}$. The exact formulas for the theoretical distribution are presented in Table 2

The summary of formulas for the final energy distributions of electrons is given in table 2. We show the expression for the same examples as in the previous table, where for the sake of simplicity we consider the scattering synchronized and aligned ($\Delta_{\parallel} = 0$, $\Delta_{\perp} = 0$). The distributions can be derived for any case (from table 1 or not) following the procedure that we just outlined.

Setup	Energy distributions after classical radiation reaction
Wide beam	$\frac{dN_b}{d\gamma} = 4\pi n_b W_0^2 z_R \frac{\gamma_0/\gamma}{\gamma_0 - \gamma} \left(\frac{L(L^2 + 16z_R^2)}{128z_R^3} \theta_1 + \frac{1}{6(\gamma_0 - \gamma)^{3/2}} (c_{RR}\gamma\gamma_0 a_0^2 + 2(\gamma_0 - \gamma)) \sqrt{c_{RR}\gamma\gamma_0 a_0^2 + \gamma - \gamma_0} (1 - \theta_1) \right)$
Thin beam	$\frac{dN_b}{d\gamma} = \frac{2N_b z_R}{L} \frac{\gamma_0}{(\gamma_0 - \gamma)^{3/2}} \frac{c_{RR}\gamma_0 a_0^2}{\sqrt{c_{RR}\gamma\gamma_0 a_0^2 + \gamma - \gamma_0}} \theta_1 \theta_2$
Short beam	$\frac{dN_b}{d\gamma} = N_b \frac{W_0^2}{2R^2} \frac{\gamma_0/\gamma}{\gamma_0 - \gamma} \left(\frac{\gamma_0 - \gamma}{c_{RR}\gamma_0 \gamma a_0^2} \right) \frac{W_0^2}{2R^2} \theta_2$

Table 2: Electron spectra after classical scattering with focused laser pulses for different beam geometries. Distributions are obtained from table 1 and the scaling law (3). The minimum electron energy is $\gamma_{\min} \equiv \gamma_0/(1 + c_{RR}\gamma_0 a_0^2)$ and the energy at branch transition is $\gamma_z \equiv \gamma_0/(1 + c_{RR}\gamma_0 a_z^2)$. $\theta_1 \equiv \theta(\gamma - \gamma_z)$, $\theta_2 \equiv \theta(\gamma - \gamma_{\min})$

3.2. Quantum Radiation Reaction and misaligned beams: semi-analytical approach

In the previous sub-section, we considered the case of deterministic, classical radiation reaction. As the laser field and the electron energy increase, the photon emission becomes stochastic due to its quantum nature and tends to spread the distribution function of the photon emitting electrons. There is no general analytical solution for the evolution of the coupled electron and photon distributions, even in the simplest field configurations. However, the plane wave case is easy to simulate numerically in one dimension. In this subsection, we show that we can use specific plane wave solutions from 1D simulations to reconstruct a more general 3D result. Similarly to the deterministic case, the energy lost to photons is expected to increase as the laser a_0 increases and the ratio R/W_0 decreases.

In figures 4 a) and b) we show simulation results for the final photon and electron spectra after scattering with a pulsed plane wave. Analogously with the classical case, there are more electrons in the low energy tail of the distribution for the high values of a_0 . To map these results to 3D, similarly to equation (4), we weight the plane wave spectra $dN^{PW}/d\gamma$ by the $a_{0,\text{eff}}$ distribution function

$$\frac{dN^{3D}}{d\gamma}(\gamma; a_0) \sim \sum_{a_{0,\text{eff}}} \frac{dN^{PW}}{d\gamma}(\gamma, a_{0,\text{eff}}) \frac{dN_b}{da_{0,\text{eff}}}(a_{0,\text{eff}}) \quad (5)$$

where $a_{0,\text{eff}}$ is a uniformly distributed, discrete set of a_0 values with enough resolution to represent the full effective intensity distribution.

By running several PW simulations in parallel, this approach can be used to calculate the asymptotic distributions expected after the interaction with a focused Gaussian laser pulse (including and all the variations on alignment), which has orders of magnitude lower computational cost than one full-scale 3D or quasi-3D simulation. In figures 4 c) and d) we present the results of quasi-3D simulations in color against the reconstruction method presented before, showing good agreement. We used PW simulations with a_0 from 0 to 12 in step increments of 0.2.

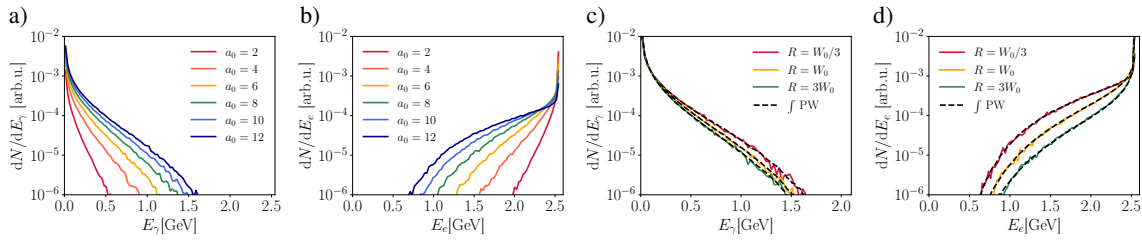


Figure 4: Reconstructing particle spectra in focused laser collisions using pulsed plane wave datasets. a) and b) photon and electron final spectra in pulsed plane wave collisions, respectively. c) and d) Final spectra from a 3D simulation of the interaction of a diffraction-limited (Gaussian) laser pulse against the reconstruction from 1D plane wave samples.

The same PW dataset can be effectively used to reconstruct the electron and photon distributions from a collision with a transverse offset (presented in figure 5).

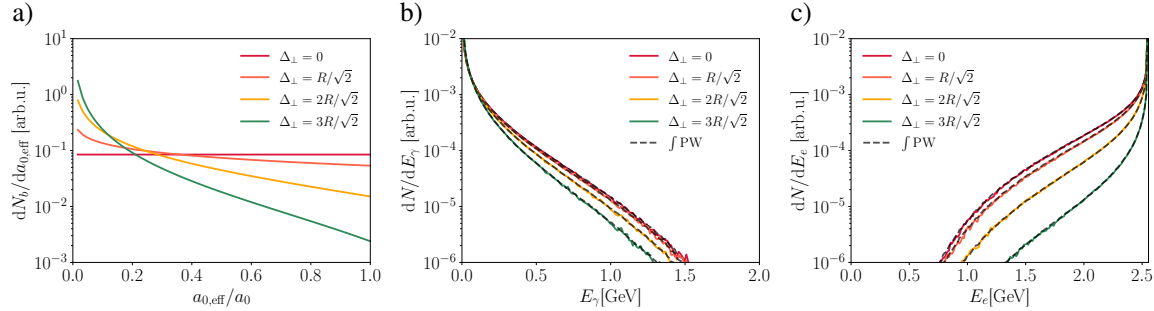


Figure 5: Perpendicular displacement of Short beam. Left: $a_{0,\text{eff}}$ distribution. Middle: photon spectra. Right: electron spectra. Same main parameters as in figure 4, with maximum $a_0 = 12$.

It is also possible to reconstruct the expected distributions for longitudinal (temporal) offsets (see figure 6).

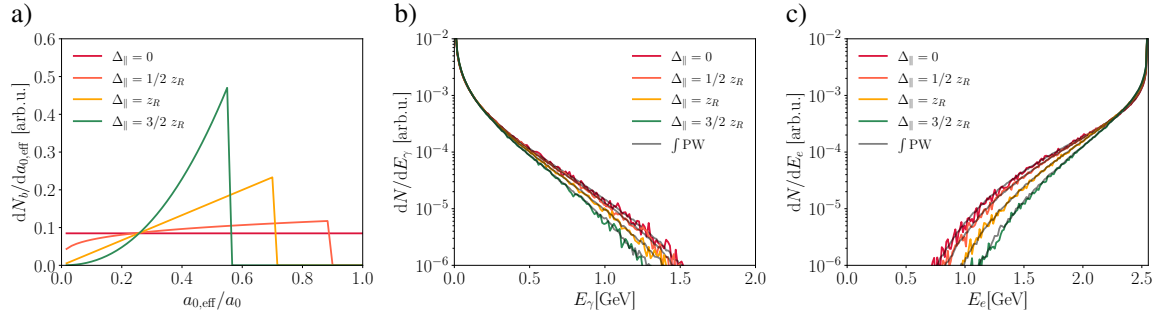


Figure 6: Parallel displacement of Short beam. Left: $a_{0,\text{eff}}$ distribution. Middle: photon spectra. Right: electron spectra. Same main parameters as in figure 4, with maximum $a_0 = 12$.

In later sections, this approach is applied to other observables from laser-beam scattering.

4. The approximate photon spectra

In this section, we discuss the possibility of computing an approximate asymptotic photon spectrum without resorting to PIC simulations. This can replace the 1D plane wave calculations of the photon spectra from the previous section.

As an electron interacts with a wavepacket, it loses energy, on average, following the semi-classical equation of motion (the Lorentz force is omitted in the equation, we just display the radiation reaction term)

$$\left(\frac{dp}{dt} \right)_{RR} = - g(\chi_e) P_{cl}/c, \quad P_{cl} = \frac{2 \alpha c}{3 \lambda_c} m_e c^2 \chi_e^2 \quad (6)$$

where $\chi_e \sim 2 \gamma a/a_S$ is the lepton quantum nonlinearity parameter; a_S is the normalized Schwinger vector potential; P_{cl} the classical synchrotron-like emitted power, α is the fine-structure constant; λ_c is the Compton wavelength, and $g(\chi_e)$ the electron Gaunt-factor (which corrects the average emitted power to be consistent with a full quantum approach).

According to equation (6), for each phase of the laser ϕ we can assign an associated average electron energy $\gamma(\phi)$ and combine this with an instantaneous laser field vector potential $a(\phi)$. For each of these pairs of values, we compute the quantum synchrotron spectrum (in local constant field approximation) and integrate them to obtain the final, cumulative photon spectrum as shown in figure 7.

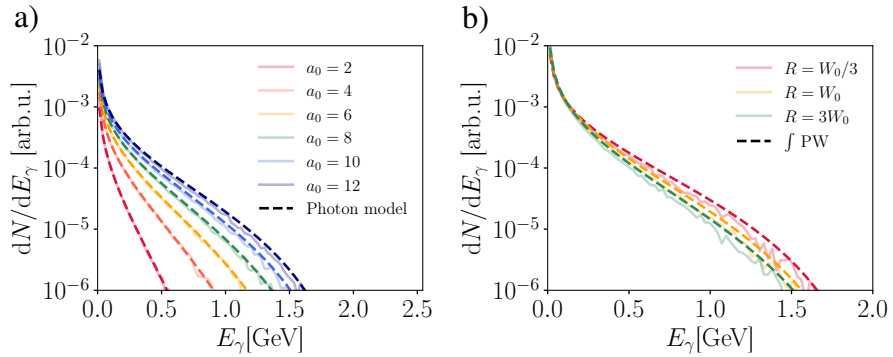


Figure 7: Left: comparison between final cumulative photon spectra in electron-laser PW interaction for varying a_0 in simulations (solid) and reconstructed (dashed). Right: comparison between final cumulative photon spectra in electron-laser PW interaction for varying R/W_0 in simulations (solid) and reconstructed (dashed).

This results in a very good estimate of the photon spectra. Figure 7 also shows small deviations between the simulations and the theoretically predicted reconstructions. These deviations can be attributed to the neglected energy spread of the photon emitting electrons. This model could be further improved by applying a Boltzmann equation solver to capture a self-consistent, multi-particle evolution of all the energy momenta.

5. Angular distribution of electrons, photons and positron yield

After having addressed the average energy, energy spread and the evolution of the electron energy distribution function during the laser-electron scattering, in this section we discuss the possibility of incorporating several scaling laws for different scattering observables into the model. In particular, the highlight is given to the angular distribution and of both electrons and photons, as this can be directly measured in experiments. For completeness, we also mention how the same method is applied to calculate the positron yield, which was addressed in more detail in our previous work [23].

5.1. Photon angular distribution

Relativistic electrons emit photons within an angle $\sim 1/\gamma$ around their propagation direction. When an electron interacts head-on with a linearly polarized laser (LP), the transverse momentum is of the order of the laser vector potential, so the expected opening angle of the emission is $\sim \langle a \rangle / \gamma$ in the polarization direction. The third direction, perpendicular both to the propagation and the polarisation still has an expected typical divergence of $\sim 1/\gamma$. Here a and γ refer to the instantaneous laser amplitude and electron energy. To account for a laser temporal envelope (in particular, we use a \sin^2 pulse envelope) and linear polarization, the average instantaneous value of the laser vector potential is twice decreased by a factor of $\sqrt{2}$ compared to the peak field. This gives an overall expected root-mean-squared photon angle of $\sim 0.5 a_0 / \gamma_0$.

For moderate to high laser intensity, the number of photons above a certain energy scales linearly with a_0 (see figure 8 a). Since the number of photons emitted by the electrons is a function of a_0 , this has to be included in the weighted average over the instantaneous emission angle to obtain the expected final divergence of the signal.

As shown in figure 8, using this information and pairing it with the effective intensity distributions allows predicting the final photon divergence for diffraction-limited laser-electron collisions, including spatio-temporal misalignment.

$$\theta_{3D}^2 \sim \int \theta_{PW}^2 \frac{N_\gamma}{N_e} \frac{dN_b}{da_{0,\text{eff}}} da_{0,\text{eff}} / \int \frac{N_\gamma}{N_e} \frac{dN_b}{da_{0,\text{eff}}} da_{0,\text{eff}} \quad (7)$$

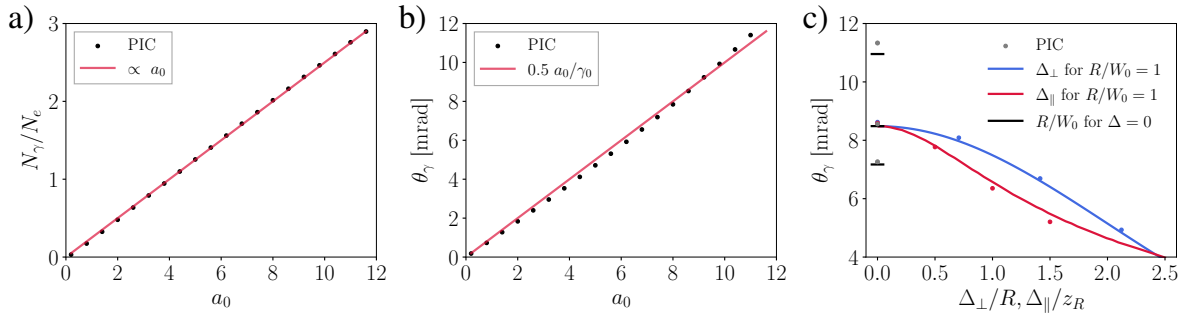


Figure 8: Left: number of photons per electron (only including photons above 1 MeV energy). Middle: photon angle rms in plane wave. Right: photon angle rms for setups using focused lasers.

5.2. Electron angular distribution

As the photon divergence depends directly on the instantaneous electron divergence at emission time, estimating the final photon divergence can be accomplished with a simple integration, as shown in previous subsection. The asymptotic electron divergence is more challenging to estimate because of the accumulated diffusion of the distribution function due to the quantum stochasticity of photon emission. In [16], a scaling law was derived for the electron transverse momentum divergence in a PW as a function of average final energy γ_f and energy spread σ_f , following the quantum radiation reaction on the emitting electrons. In [29], it was shown that if the precise values of final average energy and energy spread were used in the previously mentioned scaling law, it could accurately predict the final electron divergence. However, the estimate of the final divergence is sensitive to the accuracy of the estimates for σ_f and γ_f . The final electron divergence, measured as root-mean-squared angle in the electron momentum [16], can be written as

$$\theta_e^{PW} \sim \sqrt{\frac{2}{\pi}} \frac{a_0 \sigma_f}{\gamma_f^2} \quad (8)$$

where the electron energy spread is upper-bounded by

$$\sigma_f^2 \leq 1.455 \times 10^{-4} \sqrt{I_{22}} \frac{\gamma_0^3}{(1 + 6.12 \times 10^{-5} \gamma_0 I_{22} \tau_0[\text{fs}])^3}. \quad (9)$$

Here, $I_{22} = 10^{-22} \text{ I}[\text{W/cm}^2]$ is the laser intensity and γ_f is the final electron energy given by equation (3). Similarly to the photon divergence, the equivalent electron divergence in 3D will be the root-mean-squared plane wave divergence weighted by the $a_{0,\text{eff}}$ distribution.

In figure 9, we compare this scaling law against PIC simulations, first in the case of a plane wave for different a_0 values, and then for focused Gaussian laser scattering with different collision offsets.

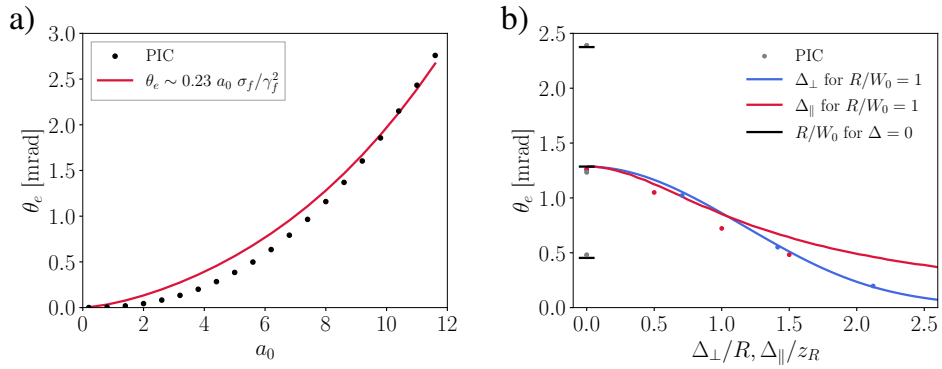


Figure 9: Left: electron angle rms in plane wave. Right: electron angle rms in focused laser setups.

Equation (9) was originally derived for scattering against a laser pulse with a long, flat temporal envelope, where sufficient time would have passed for an equilibrium between radiative cooling and stochastic diffusion to have occurred. For the laser pulse durations considered in this work ($\ll 100 \text{ fs}$), this is not always satisfied. Consequently, we correct the scaling law with a multiplicative pre-factor to match the plane wave results with a shorter interaction time. The results are presented in figure 9, where there is an overall good correspondence between the model and simulations, and once again we can incorporate the spatio-temporal misalignment.

Knowing the asymptotic divergence of the electron beam can be very useful in experiments. For example, in [30, 31], the authors explore the possibility of using the induced asymmetry in the electron angular distributions in a linearly polarized laser as a robust sign of quantum stochasticity broadening. It may also be used to estimate the peak laser intensity during scattering, which cannot be directly measured.

5.3. Positron yield in electron-laser scattering

In electron-laser scattering for pair production, both nonlinear Compton Scattering and nonlinear Breit-Wheeler pair production have to be taken into account. These two stochastic processes have to occur in succession and within the crossing time of the laser

pulse. In the *soft-shower* regime (only one generation of pairs produced), the electrons emit photons of broad spectra and at different phases of the laser. As a consequence, photons are distributed not only in energy but also in their integrated probability of decaying into pairs. This makes theoretical modeling of these events somewhat more challenging than direct photon-laser scattering.

An approximate scaling law for the positron yield (and average energy) in the scattering of electrons with a pulsed plane wave was derived in [21]. This expression can then be implemented numerically into this framework (as we have done in [23]) to estimate the positron yield in focused laser setups.

6. Conclusions

We present a semi-analytical model which offers a fast and computationally inexpensive method of predicting electron yield, photon yield, spectra and angular divergence in realistic electron scattering setups.

We introduce the model by considering the interaction between a distribution of electrons interacting with a focused intense laser pulse, assuming the probe particles perform ballistic trajectories. We then derive the closed-form electron spectra for different collision geometries after experiencing energy lost due to classical radiation reaction. Furthermore, we have shown that data from quasi-1d simulations of scattering against a plane wave with a temporal envelope can be recombined to yield the equivalent particle spectra in a focused laser setup, both for classical and quantum radiation reaction models. In both cases, the simulations and the theory agree very well, demonstrating that the presented model can be used as a cheap and fast alternative to 3D-PIC simulations. By employing scaling laws for the final photon and electron divergence in a plane wave, we have also shown that these observables scenarios can also be predicted. Besides Gaussian profiles, the model could also be extended to other beam profiles, such as Laguerre or Hermite-Gauss modes.

The need for fast computation of observables in high-repetition-rate facilities requires a robust and efficient framework. The incoherent nature of the nonlinear Compton Scattering gamma radiation (independent between different electrons, but not within a single electron trajectory) allows calculation of the final spectrum as a sum of single-particle spectra (contrary to Thomson scattering where there will be interference patterns). Having a sufficiently accurate forward model could enable the reconstruction of experimental parameters and profiles (beam and laser), and quantify the associated uncertainties. This will be particularly important in high repetition-rate facilities, where data needs to be processed quickly and can also be statistically relevant to train automated models. In the future, we will investigate this possibility.

Another possible extension of this framework is the positron production at 90° of incidence for Direct Laser Acceleration (DLA). Contrary to a head-on collision, here the energy cutoff of the electron-positron pairs is no longer limited to the initial energy of the interacting electrons. If positrons are generated at low energies, they can be

trapped, and accelerated along the laser propagation direction [32].

We strongly believe these findings will contribute to further analytical calculations on classical and quantum radiation reaction and pair production and help design future experiments to validate current models of Strong-Field QED.

7. Acknowledgments

This article comprises part of the PhD thesis work of Óscar Amaro, which will be submitted to Instituto Superior Técnico, University of Lisbon.

The authors thank Mr. B. Barbosa, Dr. B. Martinez, and Dr. L. I. Iñigo Gamiz for fruitful discussions and proofreading the manuscript. This work was supported by the European Research Council (ERC-2015-AdG Grant No. 695088) and Portuguese Science Foundation (FCT) Grants No. CEECIND/01906/2018, PTDC/FIS-PLA/3800/2021, and UI/BD/153735/2022. Simulations were performed at the IST cluster (Lisbon, Portugal).

References

- [1] Eli science and technology with ultra-intense lasers whitebook, edited by andreas thoss (2011)
- [2] Apollon URL <http://www.apollon-laser.fr/>
- [3] Corels URL https://corels.ibs.re.kr/html/corels_en/
- [4] Facet-ii URL https://portal.slac.stanford.edu/sites/ard_public/facet/Pages/FACET-II.aspx
- [5] Meuren S, Bucksbaum P H, Fisch N J, Fiúza F, Glenzer S, Hogan M J, Qu K, Reis D A, White G and Yakimenko V 2020 On Seminal HEDP Research Opportunities Enabled by Colocating Multi-Petawatt Laser with High-Density Electron Beams (*Preprint* 2002.10051)
- [6] Abramowicz H, Altarelli M, Aßmann R, Behnke T, Benhammou Y, Borysov O, Borysova M, Brinkmann R, Burkart F, Büßer K, Davidi O, Decking W, Elkina N, Harsh H, Hartin A, Hartl I, Heinemann B, Heinzl T, TalHod N, Hoffmann M, Ilderton A, King B, Levy A, List J, Maier A R, Negodin E, Perez G, Pomerantz I, Ringwald A, Rödel C, Saimpert M, Salgado F, Sarri G, Savoray I, Teter T, Wing M and Zepf M 2019 Letter of Intent for the LUXE Experiment (*Preprint* 1909.00860)
- [7] Abramowicz H, Acosta U H, Altarelli M, Assmann R, Bai Z, Behnke T, Benhammou Y, Blackburn T, Boogert S, Borysov O, Borysova M, Brinkmann R, Bruschi M, Burkart F, Büßer K, Cavanagh N, Davidi O, Decking W, Dosselli U, Elkina N, Fedotov A, Firlej M, Fiutowski T, Fleck K, Gostkin M, Grojean C, Hallford J A, Harsh H, Hartin A, Heinemann B, Heinzl T, Helary L, Hoffmann M, Huang S, Huang X, Idzik M, Ilderton A, Jacobs R M, Kaempfer B, King B, Lakhno H, Levanon A, Levy A, Levy I, List J, Lohmann W, Ma T, Macleod A J, Malka V, Meloni F, Mironov A, Morandin M, Moron J, Negodin E, Perez G, Pomerantz I, Poeschl R, Prasad R, Quere F, Ringwald A, Roedel C, Rykovanov S, Salgado F, Santra A, Sarri G, Saevert A, Sbrizzi A, Schmitt S, Schramm U, Schuwalow S, Seipt D, Shaimerdenova L, Shchedrolosiev M, Skakunov M, Soreq Y, Streeter M, Swientek K, Hod N T, Tang S, Teter T, Thoden D, Titov A, Tolbanov O, Torgrimsson G, Tyazhev A, Wing M, Zanetti M, Zarubin A, Zeil K, Zepf M and Zhemchukov A 2021 *The European Physical Journal Special Topics* **230** 2445–2560 ISSN 1951-6355, 1951-6401 (*Preprint* 2102.02032)
- [8] Excels URL <http://www.xcels.iapras.ru.>
- [9] Zeus URL <https://zeus.ingen.umich.edu>
- [10] Omega URL <https://www.lle.rochester.edu/index.php/omega-laser-facility-2/>
- [11] Hibef URL <https://www.hzdr.de/db/Cms?p0id=51491&pNid=711&pLang=en>

- [12] Cole J M, Behm K T, Gerstmayr E, Blackburn T G, Wood J C, Baird C D, Duff M J, Harvey C, Ilderton A, Joglekar A S, Krushelnick K, Kuschel S, Marklund M, McKenna P, Murphy C D, Poder K, Ridgers C P, Samarin G M, Sarri G, Symes D R, Thomas A G R, Warwick J, Zepf M, Najmudin Z and Mangles S P D 2018 *Physical Review X* **8** 011020
- [13] Poder K, Tamburini M, Sarri G, Di Piazza A, Kuschel S, Baird C D, Behm K, Bohlen S, Cole J M, Corvan D J, Duff M, Gerstmayr E, Keitel C H, Krushelnick K, Mangles S P D, McKenna P, Murphy C D, Najmudin Z, Ridgers C P, Samarin G M, Symes D R, Thomas A G R, Warwick J and Zepf M 2018 *Physical Review X* **8** 031004
- [14] Landau L 1980 *The Classical Theory of Fields* E (Butterworth-Heinemann)
- [15] Neitz N and Di Piazza A 2013 *Physical Review Letters* **111** 054802
- [16] Vranic M, Grismayer T, Fonseca R A and Silva L O 2016 *New Journal of Physics* **18** 073035 ISSN 1367-2630
- [17] Ilderton A and Torgrimsson G 2013 *Physics Letters B* **725** 481–486 ISSN 0370-2693
- [18] Vranic M, Martins J L, Fonseca R A and Silva L O 2016 *Computer Physics Communications* **204** 141–151 ISSN 0010-4655
- [19] Niel F, Riconda C, Amiranoff F, Lobet M, Derouillat J, Pérez F, Vinci T and Grech M 2018 *Plasma Physics and Controlled Fusion* **60** 094002 ISSN 0741-3335
- [20] Breit G and Wheeler J A 1934 *Physical Review* **46** 1087–1091
- [21] Blackburn T G, Ilderton A, Murphy C D and Marklund M 2017 *Physical Review A* **96** 022128
- [22] Mercuri-Baron A, Grech M, Niel F, Grassi A, Lobet M, Piazza A D and Riconda C 2021 *New Journal of Physics* **23** 085006 ISSN 1367-2630
- [23] Amaro Ó and Vranic M 2021 *New Journal of Physics* **23** 115001 ISSN 1367-2630
- [24] Badiali C, Bilbao P J, Cruz F and Silva L O 2022 *Journal of Plasma Physics* **88** 895880602 ISSN 0022-3778, 1469-7807
- [25] Montefiori S and Tamburini M 2023 SFQEDtoolkit: A high-performance library for the accurate modeling of strong-field QED processes in PIC and Monte Carlo codes (*Preprint* 2301.07684)
- [26] Fonseca R A, Silva L O, Tsung F S, Decyk V K, Lu W, Ren C, Mori W B, Deng S, Lee S, Katsouleas T and Adam J C 2002 OSIRIS: A Three-Dimensional, Fully Relativistic Particle in Cell Code for Modeling Plasma Based Accelerators *Computational Science — ICCS 2002* Lecture Notes in Computer Science ed Sloot P M A, Hoekstra A G, Tan C J K and Dongarra J J (Berlin, Heidelberg: Springer) pp 342–351 ISBN 978-3-540-47789-1
- [27] Piazza A D 2008 *Letters in Mathematical Physics* **83** 305–313 ISSN 1573-0530
- [28] Vranic M, Martins J L, Vieira J, Fonseca R A and Silva L O 2014 *Physical Review Letters* **113** 134801
- [29] Vranic M, Grismayer T, Meuren S, Fonseca R A and Silva L O 2019 *Physics of Plasmas* **26** 053103 ISSN 1070-664X
- [30] Tamburini M 2020 On-shot diagnostic of electron beam-laser pulse interaction based on stochastic quantum radiation reaction (*Preprint* 2007.02841)
- [31] Hu G, Sun W Q, Li B J, Li Y F, Wang W M, Zhu M, Hu H S and Li Y T 2020 *Physical Review A* **102** 042218
- [32] Vranic M, Klimo O, Korn G and Weber S 2018 *Scientific Reports* **8** 1–11 ISSN 2045-2322

Appendix A: PIC simulation parameters

q-scatter (quick-scattering-toolkit) is an open-source library written in Python. Examples showing its usage are provided on GitHub at: <https://github.com/0sAmaro/q-scatter>

In this appendix we specify the parameters of the simulations referred in this work. Unless specified, common to all simulations are the electron energy $\gamma_0 = 5000$, a laser

wavelength of $\lambda = 0.8$ micron ($\omega_0 = 2.35 \times 10^{15} \text{ s}^{-1}$), linear polarization, a temporal envelope of the type \sin^2 , and a corresponding rise time of the pulse of $50 \text{ } 1/\omega_p$. Additionally, when applicable, the laser spotsize was $18.85 \text{ } c/\omega_p$ and focused at the center of the simulation box. All macro-electrons and photons from the simulations are included in the particle distributions shown in the different plots of this work.

In section 3.1, we consider setups where the classical model of radiation reaction is applied. For both the Wide and Thin beam geometries, the quasi-3d simulation box dimensions were $1100 \text{ } c/\omega_p$ and $100 \text{ } c/\omega_p$ with 5500 and 500 grid cells in the longitudinal and transverse directions, respectively. The time step was $\text{dt} = 0.02 \text{ } 1/\omega_p$ and particle information was retrieved at $\text{tmax} = 320 \text{ } 1/\omega_p$ (after interaction with the laser). The electron beam profile was flat top, with dimensions $356 \text{ } c/\omega_p$ and $80 \text{ } c/\omega_p$ in the Wide beam geometry, and with 20 particles-per-cell (ppc). For the Thin beam, the transverse dimension was much smaller than the laser spot size. In the case of the Short beam, the quasi-3d box dimensions were $300 \text{ } c/\omega_p$ and $100 \text{ } c/\omega_p$, with grid cells 1500 and 500, with a time step of $\text{dt} = 0.02 \text{ } 1/\omega_p$, and a total duration of $\text{tmax} = 120 \text{ } 1/\omega_p$. The electron beam profile was flat top longitudinally, with length $0.8 \text{ } c/\omega_p$, and Gaussian in the transverse direction, with radiae $13.33 \text{ } c/\omega_p$ and $6.67 \text{ } c/\omega_p$ for the different R/W_0 ratios, and $\text{ppc}=320$.

In section 3.2 we consider the quantum model of radiation reaction. For the quasi-1d simulations, the box size was $200 \text{ } c/\omega_p$ with 2500 grid cells, a time step of $\text{dt} = 0.021 \text{ } 1/\omega_p$, and a total duration of $\text{tmax} = 130 \text{ } 1/\omega_p$. The electron density was flat top with length $4 \text{ } c/\omega_p$, and $\text{ppc}=4000$. In the case of the synchronized Short Beam setup, the quasi-3d simulation box and temporal parameters were the same as in the Short beam with classical radiation reaction. The electron density profile was Gaussian in the transverse direction, radiae 13.33 , 26.66 and $39.99 \text{ } c/\omega_p$ respectively, and $\text{ppc}=320$. For the Short beam with parallel offset, the quasi-3d simulation box dimensions were $1100 \text{ } c/\omega_p$ and $100 \text{ } c/\omega_p$ with 5500 and 500 grid cells in the longitudinal and transverse directions, respectively. The time step was $\text{dt} = 0.02 \text{ } 1/\omega_p$ and particle information was retrieved at $\text{tmax} = 120 \text{ } 1/\omega_p$. The electron Gaussian density profile had a radius of $13.33 \text{ } c/\omega_p$, with the initial center of the beam varying in the longitudinal direction in multiples of $89 \text{ } c/\omega_p$ for different offsets. In the case of the perpendicular offset, the simulation box had dimensions $300 \text{ } c/\omega_p$ in the longitudinal direction and $240 \text{ } c/\omega_p$ in both transverse directions, with 3000 and 1200 grid cells, respectively. Temporal resolution was $\text{dt} = 0.02 \text{ } 1/\omega_p$, with $\text{tmax} = 120 \text{ } 1/\omega_p$. The electron density profile was flat top in the longitudinal direction with length $0.8 \text{ } c/\omega_p$, and Gaussian in the transverse direction with radius $13.33 \text{ } c/\omega_p$. The initial center of the electron beam was varied along the x2 direction in multiples of $13.33 \text{ } c/\omega_p$ for different offsets, and $\text{ppc}=8$.